Synthesis and characterization of a novel lanthanum (III) complex with a di(2-picolyl)amine-based ligand endowed with fluorescent properties

Greta Colombo Dugoni,[a,§] Matteo Mori [b,§], Valentina Dichiarante,[a] Alessandro Sacchetti [a,*], and Fiorella Meneghetti [b]

[a] *Department of Chemistry, Materials and Chemical Engineering "Giulio Natta", Polytechnic University of Milan, Piazza Leonardo da Vinci 32, 20133 Milano, Italy.*
[b] *Department of Pharmaceutical Sciences, University of Milan, via L. Mangiagalli 25, 20133 Milano; Italy.*

([§] These authors contributed equally)

Abstract

In this work, 1-(1-benzyl-1*H*-1,2,3-triazol-4-yl)-*N*,*N*-bis(pyridin-2-ylmethyl)methanamine (**1**), a ligand belonging to the DPA family, was coordinated to La(III), yielding compound **La-1**. The structural and spectroscopic properties of the complex were analyzed by experimental and theoretical methods. The structural characterization of **La-1** was described by means of single-crystal X-ray diffraction (SC-XRD) and Hirshfeld surface analysis, allowing a detailed conformational investigation. The lowest-energy conformer obtained from DFT calculations conformationally agreed with the structure obtained by SC-XRD. ^{1}H NMR titration studies confirmed the formation of a stable complex in solution. Ligand **1** exhibited a sensitive fluorescence enhancement and ratiometric response to La(III) ions, indicating that **1** can be considered a first step towards the design of new tools for the detection of lanthanide metal ions in environmental chemistry.

Keywords

Lanthanum-complex; Crystal structure; NMR titration; Density functional theory (DFT) calculations; Fluorescence

Highlights

- A novel complex (**La-1**) based on La(III) was prepared.
- **La-1** was characterized by means of structural and spectroscopic analyses, and computational calculations.
- **La-1** displayed fluorescent properties

1. Introduction

Lanthanum is a member of the rare earth elements (REEs), a group of 17 transition metals sharing similar physical and chemical properties [1]. Lanthanum is the most abundant among REEs and has found many applications in several fields, including agriculture, water treatment, medicine, catalysis, and industry [2–5]. Despite being generally regarded as safe, comprehensive, definitive studies regarding its toxicity are still lacking. In detail, its potential for accumulation should be deemed as a serious cause of concern for both primitive and higher organisms. Lanthanum is mostly hazardous in working areas, where dusts and fumes can be inhaled, causing lung embolism and interstitial pneumoconiosis, especially after a long-term exposure [6]. Moreover, it strongly accumulates in several tissues, especially in the liver, brain, and muscles, leading to various disorders [3,7–10]. Genotoxicity of lanthanum in human peripheral blood lymphocytes was also reported [11].

Due to the increasing utilization of lanthanum complexes in industry, La(III) detection has recently gained much attention. Lanthanum is dumped in the environment mainly by petrol-producing industries [12], but it can also be dispersed when household equipment is thrown away improperly [12]. As a result, lanthanum

gradually accumulates in soil, water, and plants [1,13,14]; moreover, its presence in the marine ecosystem has been shown to be extremely damaging to a variety of aquatic creatures [15].

One of the most efficient strategies for the detection and removal of La(III) could be the formation of metal-organic complexes by means of chelating agents. In this regard, di(2-picolyl)amine (DPA) ligands may become appealing candidates; having three nitrogen atoms in their scaffold, they are excellent chelating agents, suitable for many applications in several fields, including catalysis [16–18] and biomedicine [19–21].

Notably, due to their multidentate features, DPAs have a great relevance as ligands for the coordination of both d- and f-block elements [22]. Therefore, DPA derivatives may be able to efficiently coordinate La(III) ions, possibly yielding chemosensors capable of providing real-time temporal and spatial information on lanthanum content in a variety of environments.

In the last decades, DPAs have been modified to incorporate triazole moieties to enhance their coordination ability towards various metals. Moore *et al.* [**10.1039/b921413e**] reported a "click" chemistry approach to provide suitable compounds for the coordination of heavy transition metals (Re, ^{99m}Tc), leading to innovative imaging tools for the diagnosis of prostate cancer. A similar synthetic strategy was adopted by Weisser *et al.* to investigate the coordination of tris[(1-benzyl-1*H*-1,2,3-triazol-4-yl)-methyl]amine with Ru(II) [**10.1002/chem.201303640**, **10.1002/chem.201406441]**. The authors found that the substituents at the triazole ring could be readily changed, thus allowing for the easy variation of the steric demand, the introduction of additional donors, and the anchoring of complexes on surfaces. Moreover, structural comparisons showed that triazoles bind closer to the metal center than pyridines, further supporting the use of this ligand family as a promising platform for the design and tuning of catalysts. In a recent work, the same research group expanded this class of compounds to include thermo- and photoreactive-derivatives for different synthetic applications [**10.1021/ic502807d**]. With the aim of optimizing catalysts for the copper-catalyzed azide-alkyne cycloaddition (CuAAC) reaction, Presolski *et al.* described the mixing of 1,2,3-triazolyl, 2-benzimidazoyl, and 2-pyridyl binding motifs as metal ligands [**10.1021/ja105743g**]. Interestingly, they found that the use of a triazoles provided more active catalysts. Gonzalez Cabrera *et al.* broadened the study of the coordination potential of these compounds, using a variety of metal ions, including Cu, Cr, Zn, Fe, and Co [**10.1039/b713501g**]. The authors set-up a transition metal-tolerant CuAAC protocol for the synthesis of mono- and bis-metallated[2]rotaxanes, developing a versatile methodology for appending a metal ion or complex to an organic scaffold. A modification of the same reaction was also studied by Zhu *et al.*, who developed an optimized procedure without the addition of reducing agents to simplify the isolation of highly polar polyaza compounds [**10.1021/ol9021113**]. Overall, these works support the importance of DPAs, conveniently decorated with a 1,2,3-triazole substituent, as versatile ligands for the coordination of different transition metals.

In the framework of our studies of metal-organic compounds [18,23,24], we report here our recent investigations on the coordination of 1-(1-benzyl-1*H*-1,2,3-triazol-4-yl)-*N*,*N*-bis(pyridin-2-ylmethyl)methanamine (**1**, Chart 1) to an inorganic lanthanum salt (lanthanum(III) nitrate). The structural and spectroscopic properties of the new complex (**La-1**) were analyzed by experimental methods and theoretical calculations. In addition, inspired by previous works [25–27], we decided to investigate the luminescence of the ligand and the effects of the complexation with La(III) by fluorescence titration studies. Our studies will contribute to expand the knowledge on the coordination potential of 1,2,3-triazolyl-functionalized DPAs, laying the foundations for further investigations on the chelation of lanthanides. Moreover, our preliminary data on the fluorescence of the **La-1** complex may inspire the development of a novel molecular sensor for the smart detection of lanthanum in different media.

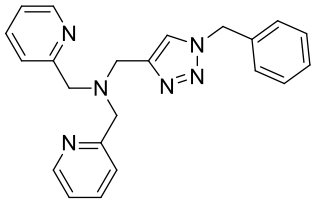

Chart 1. Molecular structure of 1-(1-benzyl-1*H*-1,2,3-triazol-4-yl)-*N*,*N*-bis(pyridin-2-ylmethyl)methanamine (**1**).

2. Materials and methods

2.1. General

All starting materials and solvents were acquired from commercial sources (Merck KGaA, Darmstadt, Germany) and used as received for all synthetic purposes. Solvents employed in titration measurements were purified by standard procedures. All ^{1}H NMR spectra were recorded on a 400 MHz Brüker (Billerica, Massachusetts, USA) NMR spectrometer. ESI–MS spectra were acquired on a Bruker Esquire 3000 PLUS instrument (ESI Ion Trap LC/MSn System; Bruker, Billerica, MA, USA), equipped with an ESI source and a quadrupole ion trap detector (QIT). Microwave reactions were conducted in a Biotage® Initiator+ (Uppsala, Sweden). Fluorescence spectra were recorded at room temperature on a Varian Cary Eclipse fluorescence spectrometer.

2.2. Synthesis

N-(2-Pyridilmethyl)-2-pyridylmethanimine (**2**). To a suspension of Na_2SO_4 (3940 mg, 27.74 mmol, 6 eq) in dry THF (9.24 mL) was added pyridine-2-carbaldehyde (500 mg, 4.62 mmol, 1 eq), followed by 2-aminomethylpyridine (495 mg, 4.62 mmol, 1 eq). The mixture was stirred at room temperature for 12 h under N_2 atmosphere. After the elimination of the solid by filtration, the solvent was evaporated under reduced pressure to afford the desired product as a yellow oil (yield: 92.8%). ^{1}H NMR (400 MHz, $CDCl_3$) δ 8.67 (ddd, *J* = 4.9, 1.8, 1.0 Hz, 1H, 6'-Pyr), 8.61 – 8.56 (m, 2H, 6'-Pyr and CH-Pyr), 8.09 (dt, *J* = 7.9, 1.1 Hz, 1H, 3'-Pyr), 7.79 – 7.73 (m, 1H, 4'-Pyr), 7.68 (td, *J* = 7.7, 1.8 Hz, 1H, 4'-Pyr), 7.42 (d, *J* = 7.8 Hz, 1H, 3'-Pyr), 7.33 (ddd, *J* = 7.5, 4.9, 1.3 Hz, 1H, 5'-Pyr), 7.19 (ddd, *J* = 7.6, 4.9, 1.2 Hz, 1H, 5'-Pyr), 5.03 (d, *J* = 1.5 Hz, 2H, CH_2-Pyr). Anal. calcd. for $C_{12}H_{11}N_3$: C, 73.07; H, 5.62; N, 21.30; found: C, 73.10; H, 5.81; N, 21.09. ESI-MS (*m*/*z*) calcd. for $C_{12}H_{11}N_3$: 397.1; found: 398.1 $[M+H]^+$.

*Di(2-picolyl)amine (**3**).* *N*-(2-Pyridilmethyl)-2-pyridylmethanimine (1824 mg, 9.25 mmol, 1 eq) was dissolved in MeOH (15 mL), and $NaBH_4$ (350 mg, 9.25 mmol, 1 eq) was added slowly at 0 °C. After 10 min, the mixture was stirred at room temperature for 5 h. Then, the reaction mixture was filtered, and the solvent was evaporated, giving the desired product as a yellow oil (yield: 65%). ^{1}H NMR (400 MHz, $CDCl_3$) δ 8.57 – 8.55 (m, 2H, 6'-Pyr), 7.66 – 7.62 (m, 2H, 4'-Pyr), 7.36 (d, *J* = 7.8 Hz, 2H, 3'-Pyr), 7.17 – 7.14 (m, 2H, 5'-Pyr), 3.98 (s, 4H, CH_2-Pyr). Anal. calcd. for $C_{12}H_{13}N_3$: C, 72.33; H, 6.58; N, 21.09; found: C, 72.37; H, 6.62; N, 21.01.

*N-Propargyl-di(2-picolyl)amine (**4**).* To a suspension of K_2CO_3 (1274 mg, 9.5 mmol, 3.8 eq) in dry THF (12.5 mL) was added di(2-picolyl)amine (**3**) (500 mg, 2.5 mmol, 1 eq), followed by propargyl bromide (446 mg, 3.75 mmol, 1.5 eq). The mixture was stirred at room temperature for 12 h under N_2 atmosphere. After the elimination of the solid by suction, the solvent was evaporated under vacuum, affording the desired product as a brown oil (yield: 88%). ^{1}H NMR (400 MHz, $CDCl_3$) δ 8.56 (ddd, *J* = 4.9, 1.7, 0.8 Hz, 2H, 6'-Pyr), 7.66 (td, *J* = 7.7, 1.8 Hz, 2H, 4'-Pyr), 7.52 (d, *J* = 7.8 Hz, 2H, 3'-Pyr), 7.17 (ddd, *J* = 7.4, 4.9, 1.0 Hz, 2H, 5'-Pyr), 3.94 (s, 4H, CH_2-Pyr), 3.44 (d, *J* = 2.4 Hz, 2H, CH_2-Propargyl), 2.29 (t, *J* = 2.4 Hz, 1H, CH-Propargyl).

*(Azidomethyl)benzene (**5**)*. Benzyl bromide (1000 mg, 5.8 mmol, 1 eq) and NaN_3 (754 mg, 11.6 mmol, 2 eq) were dissolved in DMF (12 mL) and heated to 100 °C under microwave irradiation for 15 min. The reaction mixture was extracted with AcOEt, and the collected organic layers were washed with brine and dried with

Na_2SO_4. The solvent was evaporated under vacuum to give the desired product, without any further purification (yield: 73%). ^{1}H NMR (400 MHz, $CDCl_3$) δ 7.35 – 7.22 (m, 5H, Ph), 4.27 (s, 2H, CH_2-Ph).

*1-(1-Benzyl-1H-1,2,3-triazol-4-yl)-N,N-bis(pyridin-2-ylmethyl)methanamine (**1**)*. *N*-Propargyl-di(2-picolyl)amine (**4**) (200 mg, 0.8 mmol, 1 eq), (azidomethyl)benzene (**5**) (123 mg, 0.9 mmol, 1.1 eq), Na ascorbate (134 mg, 0.7 mmol, 0.8 eq), and $CuSO_4$ (54 mg, 0.3 mmol, 0.4 eq) were dissolved in a 1:1 mixture of acetone and water (4.4 mL). The reaction was performed under microwave irradiation at 50 °C for 1 h. Then, the mixture was extracted with EtOAc, and the collected organic layers were washed with 1M NH_3 and dried with Na_2SO_4. The solvent was evaporated under vacuum to afford the desired product without any further purification (yield: 73%). ^{1}H NMR (400 MHz, $CDCl_3$) δ 8.54 (ddd, *J* = 4.9, 1.8, 0.9 Hz, 2H, 6'-Pyr), 7.67 (td, *J* = 7.6, 1.8 Hz, 3H, 4'-Pyr and CH-Triazole), 7.58 (d, *J* = 7.8 Hz, 2H, 3'-Pyr), 7.44 – 7.33 (m, 5H, Ph), 7.20 – 7.15 (m, 2H, 5'-Pyr), 5.53 (s, 2H, CH_2-Ph), 3.97 (s, 2H, CH_2-Triazole), 3.94 (s, 4H, CH_2-Pyr). ^{13}C NMR (400 MHz, $CDCl_3$) δ 159.00, 149.50, 136.76, 123.42, 122.38, 73.89, 59.72, 42.79; Anal. calcd. for $C_{22}H_{22}N_6$: C, 71.33; H, 5.99; N, 22.69; found: C, 71.37; H, 6; N, 22.65. ESI-MS (*m/z*) calcd. for $C_{22}H_{22}N_6$: 370.2; found: 371.2 $[M+H]^+$, 393.2 $[M+Na]^+$.

2.3. X-ray crystallographic data collection and structure determination

Suitable crystals for SC-XRD analysis were grown by slow evaporation of a solution of **1** and $La(NO_3)_3$ in acetonitrile, after one week at room temperature. Diffraction data were acquired on a Bruker-AXS CCD-based three-circle diffractometer (Bruker, Billerica, MA, USA), working at ambient temperature with graphite-monochromatized Mo-Kα X-radiation (λ = 0.7107 Å).

SC-XRD data in the ϑ range 2-30° were collected acquiring five sets of 600 bidimensional CCD frames with the following operative conditions: omega rotation axis, scan width 0.3°, acquisition time 20 s, sample-to-detector distance 60 mm, ϕ angle fixed at five different values (0°, 90°, 150°, 200°, 340°) for the five different sets.

Omega-rotation frames were processed with the SAINT software [28] for the data reduction (including intensity integration, background, Lorentz, and polarization corrections) and for the determination of accurate unit-cell dimensions, obtained by least-squares refinement of the positions of 9917 independent reflections with $I > 10\sigma(I)$ in the ϑ range 2-25°. Absorption effects were empirically evaluated by the XABS2 software [29], and an absorption correction was applied to the data (0.653 and 0.847 min and max transmission factor).

The structure was solved by direct methods using SIR-2014 [30] and completed by iterative cycles of full-matrix least-squares refinement on F_0^2 and ΔF synthesis using SHELXL-18/3 [31] on the WingX.v2014.1 suite [32]. Hydrogen atoms were introduced at calculated positions in their described geometries and allowed to ride on the attached atom with fixed isotropic thermal parameters (1.2 U_{eq} of the parent atom for aromatic and methylene groups). The structure was analyzed by PARST [33] and Mercury 2020.2.0 [34]; the graphical representations were rendered with Mercury [34]. Hirshfeld surface (HS) analysis was performed with CrystalExplorer 21 [35]. CCDC entry 2058917 contains the supplementary crystallographic data for this paper. A summary of the data collection and refinement statistics is reported in Table S1 (Supplementary Material).

3. Results and discussion

3.1. Synthesis

Ligand **1** was prepared following a slightly modified literature procedure [18] and fully characterized by NMR spectroscopy, mass spectrometry, and elemental analysis. In Scheme 1, the complete synthetic pathway is described, starting with the reductive amination of pyridine-2-carbaldehyde with 2-aminomethylpyridine, in the presence of sodium borohydride as the reducing agent. Considering the poor stability of the resulting secondary amine (**3**), the product could not be adequately stored and was directly used in the next step. The

N-alkylation of the intermediate, carried out in basic conditions with propargyl bromide, yielded the alkyne **4**, which was finally reacted with benzylazide in a CuAAC 1,3 dipolar cycloaddition to afford the desired compound **1**. The reaction was performed in classical "click" conditions, using sodium ascorbate and copper sulphate in a mixture of acetone-water 1:1. Microwave irradiation at 50 °C for 1 h was employed to shorten the duration of the reaction and reduce the formation of byproducts. After some attempts, dichloromethane was selected as the best extraction solvent for the reaction mixture, proving to be superior to other options, including ethyl acetate [18].

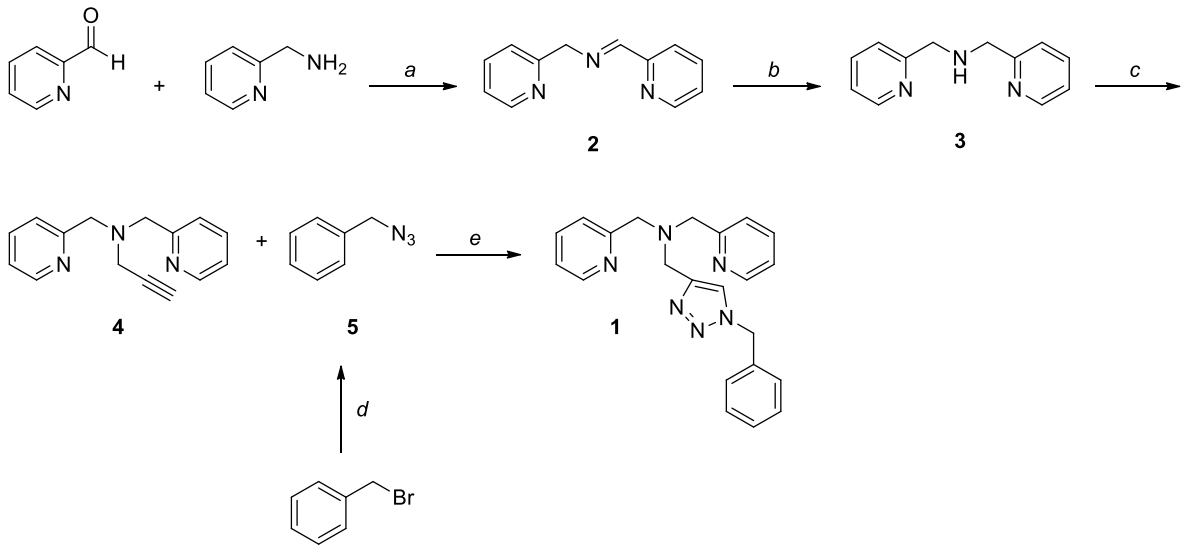

Reagents and conditions: *a*) Na_2SO_4, THF, 12 h, rt; *b*) $NaBH_4$, MeOH, 5 h, 0 °C to rt; *c*) propargyl bromide, K_2CO_3, THF, 12 h, rt, N_2 atm.; *d*) NaN_3, DMF, 15 min., 100 °C, MW; *e*) Na ascorbate, $CuSO_4$, Acetone-H_2O 1:1, 1 h, 50 °C, MW.

Scheme 1. Synthetic procedure for the preparation of **1**.

3.2. Crystal structure determination

A crystal of the complex **La-1** suitable for SC-XRD analysis was obtained by the slow crystallization of ligand **1** and $La(NO_3)_3$, dissolved in acetonitrile. An ORTEP [32] view of **La-1**, along with the adopted numbering scheme, is reported in Figure 1. The complex crystallized in the monoclinic system, space group $P2_1/c$, with one independent neutral [La-**1**$(NO_3)_3$] molecule in the asymmetric unit.

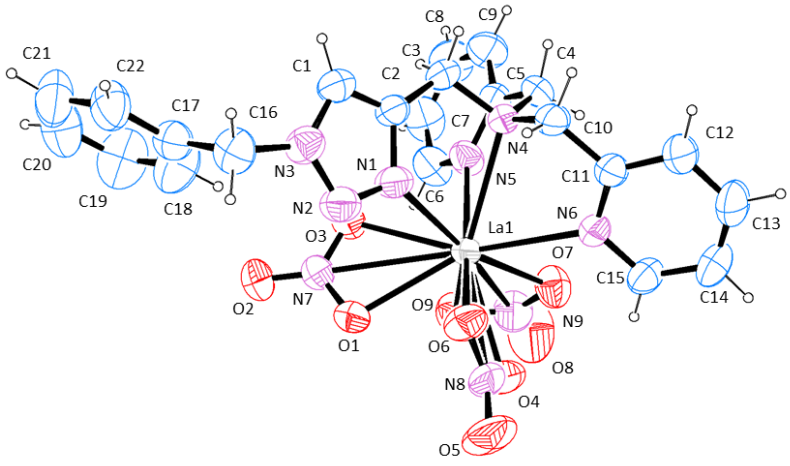

Fig. 1. ORTEP [32] plot of the crystal structure of **La-1** with the relative arbitrary atom-numbering scheme. Displacement ellipsoids are drawn at 30% probability level; H atoms are represented as spheres of arbitrary radii.

The DPA derivative **1** acts as a tetradentate ligand, coordinating the La(III) ion with four nitrogen atoms, namely N1, N4, N5, and N6. The coordination sphere is completed by three *O*,*O*′-bidentate nitrate groups. Hence, the coordination number of the La(III) atom is ten, and the polyhedron approximates a dodecahedron (Figure 2). The average La−O and La-N distances and angles (Table 2) are in agreement with literature data [36]; a comparison between experimental and theoretical values is provided in Table 1 (section 3.4).

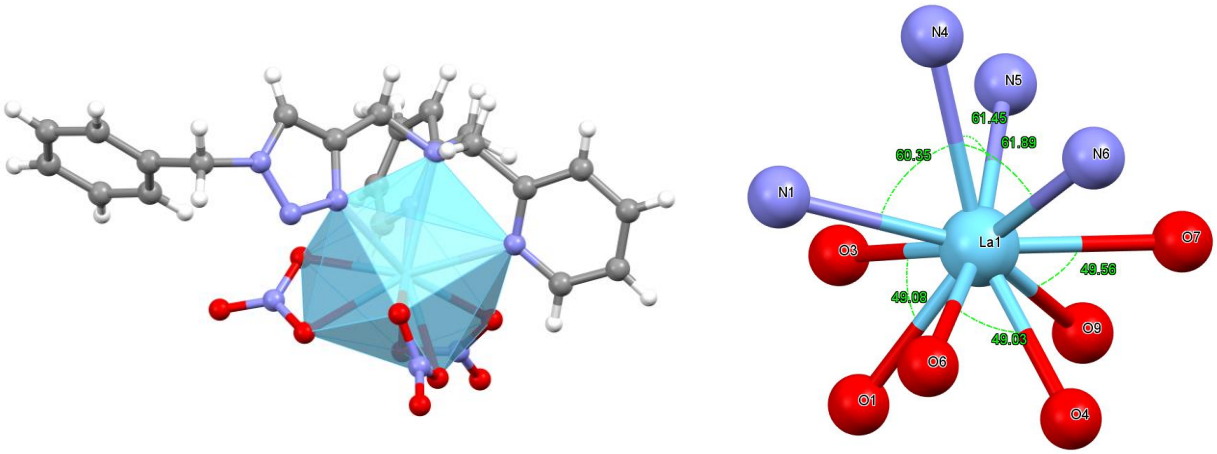

Fig. 2. Left: 3D view of **La-1**, with evidenced the coordination polyhedron of the La(III) atom. Right: details of the La(III) coordination sphere, highlighting the angles between La and the coordinated atoms.

The crystal packing of **La-1** is represented in Figure 3. The complex is extended into a supramolecular network structure *via* nonclassical hydrogen bonds between aromatic CH groups of the 1-(1-benzyl-1*H*-1,2,3-triazol-4-yl)-*N*,*N*-bis(pyridin-2-ylmethyl)methanamine and O atoms of neighboring nitrate groups. Weak π-π stacking interactions and C-H···π contacts contribute to stabilize the 3D network. In detail, the N5-C5-C6-C7-C8-C9 pyridine rings of two adjacent molecules are involved in a long-range parallel displaced stacking, characterized by an interplanar distance of 3.99(4) Å. The centroids are located at 1.37(5) Å from the C atom opposite to the N and are separated by a distance of 4.48(6) Å; the angle between the centroid-centroid vector and the plane normal is 25.2(9)°. The benzyl rings and the N6-C11-C12-C13-C14-C15 pyridine are too inclined with respect to each other to form any significant interaction, except for some C-H···π contacts. The same can be said for the N5- and N6-pyridines of nearby molecules.

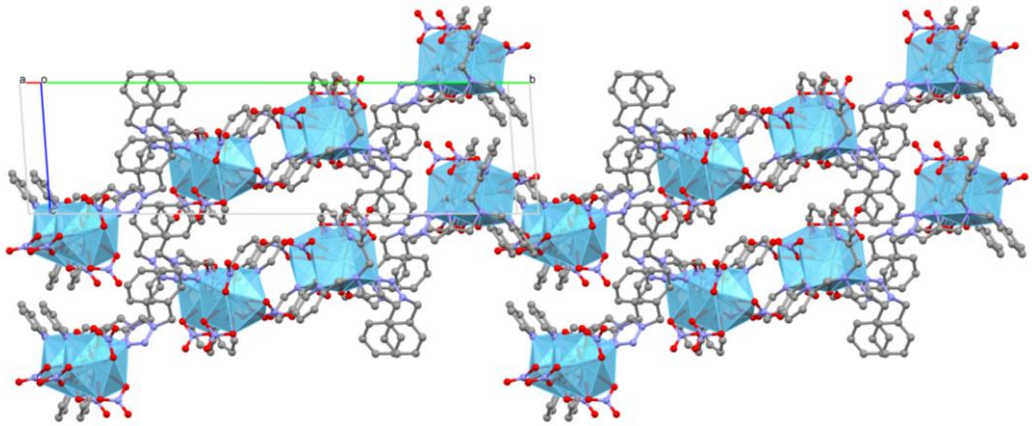

Fig. 3. Packing diagram of **La-1**, viewed along the *a* axis. Hydrogens are omitted for the sake of clarity.

A summary of the H-bonds established within the crystal structure is reported in Table S2, along with a complete account of their geometry, as calculated by PARST [33].

3.3. Hirshfeld surface (HS) analysis

The HS of **La-1** was mapped over the normalized contact distance (d_{norm}), according to the following equation:

$$d_{norm} = \frac{d_i - r_i^{vdW}}{r_i^{vdW}} + \frac{d_e - r_e^{vdW}}{r_e^{vdW}}$$

where d_i is the distance between the HS and the nearest nucleus inside the surface, d_e is the distance between the HS and the nearest nucleus outside the surface, and r^{vdW} represents the van der Waals radius of the atom. The calculated HS had the following characteristics: V = 679.57 A^3, A = 515.18 A^2, G = 0.726, Ω = 0.095. The d_{norm} property was visualized with a red-blue-white color scheme, based on the length of the intermolecular contact with respect to the sum of the van der Waals radii. As shown in Figure 4, the surface presents numerous, generally feeble red spots, corresponding to the weak H-bonds between aromatic CHs and the O atoms of the nitrate groups. The two-dimensional (2D) fingerprint of the HS, providing a visual summary of the contribution of each contact type and the relative area of the surface corresponding to it, revealed that O···H, C···H, and H···H contacts are dominant. The faint spikes pointing towards the lower left of the plot confirmed the presence of only weak H bonds. The shape of the spot corresponding to C···C contacts, protruding towards the upper right of the plot, as well as the absence of green areas, indicate weak-to-very-weak stacking interactions. The HS of **La-1** mapped over the shape-index (SI) and the curvedness is also reported in Figure 4. As evidenced by the SI, the molecular surface presents diffused bumps and hollows, which are intrinsic to the disposition of the ligand and nitrate groups around the central La(III) atom, as a result of the formation of the complex. The curvedness plot showed a slight prevalence of edges, with a few flat regions, where the stacking interactions take place.

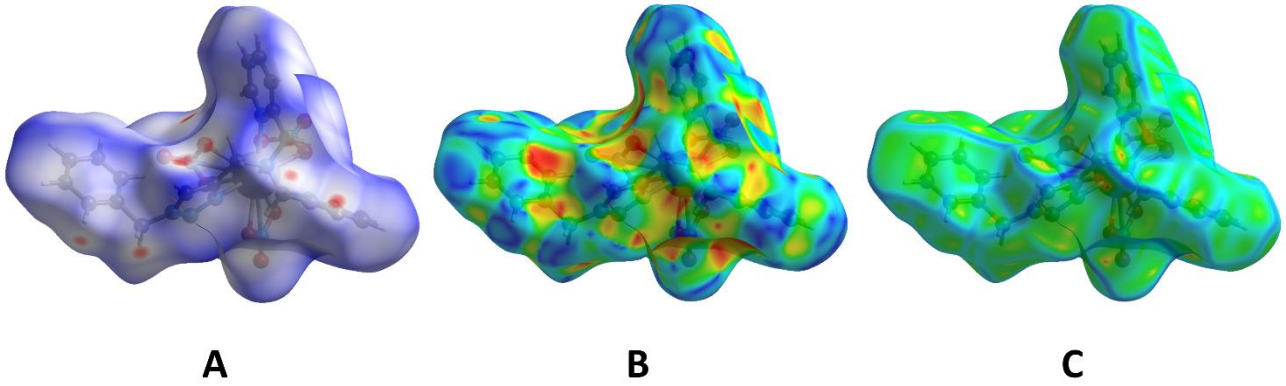

Fig. 4. A. HS of **La-1** mapped over d_{norm} with a fixed color scale in the range -0.1729 au (red) – 1.5281 au (blue), based on the length of the intermolecular contacts with respect to the sum of the van der Waals radii (red: shorter; blue: longer; white: same). **B.** HS mapped over the shape-index (color scale: -0.9967 au – 0.9966 au). Blue areas represent bumps and red regions indicate hollows. **C.** HS mapped over the curvedness (color scale: -3.6571 au – 0. 5237 au). Green represents flat regions and blue indicates edges.

In Figure 5, the main 2D fingerprint plots of the HS were reported, which specify the relative contribution of the various interaction types to the surface.

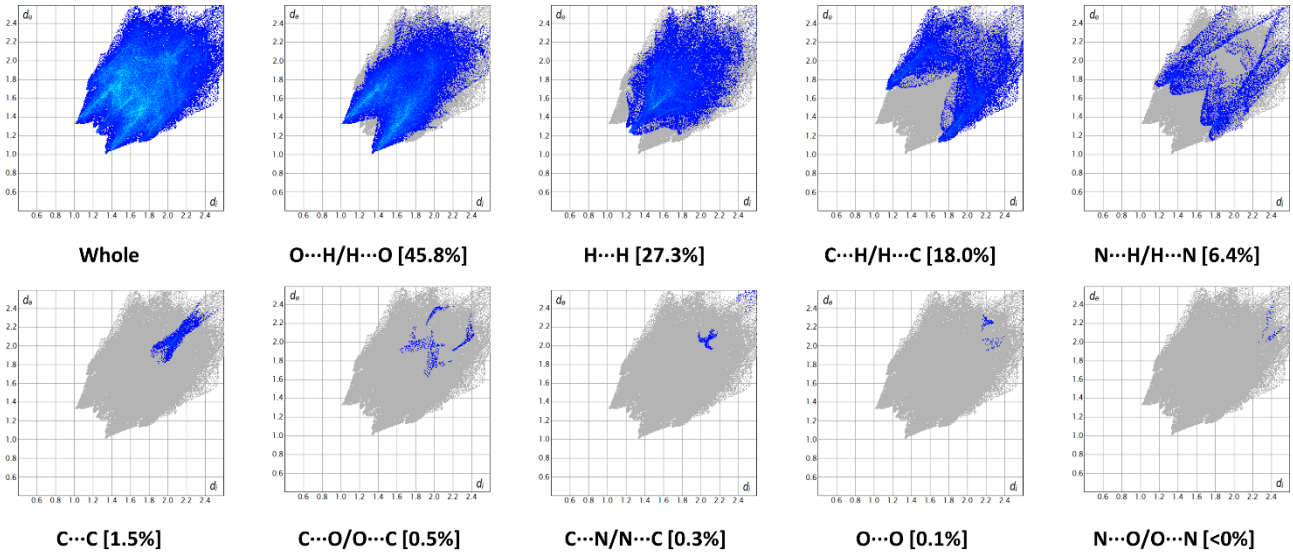

Fig. 5. 2D Fingerprint plots of **La-1**, providing a visual summary of the frequency of each combination of d_e and d_i across the HS. Points with a contribution to the surface are colored blue for a small contribution to green for a great contribution.

3.4. Computational studies

The gas phase structures of **1** and its corresponding La(III) complex were investigated by computational methods. After a conformational analysis with a Monte Carlo search and MM minimization, the first two minimum energy conformers were optimized by DFT calculations, at the B3LYP level of theory, using the LANL2DZ basis set. The optimized structures of the lowest- and first higher-energy conformers of **La-1** (ΔE = 0.6 kcal/mol) are shown in Figure 6.

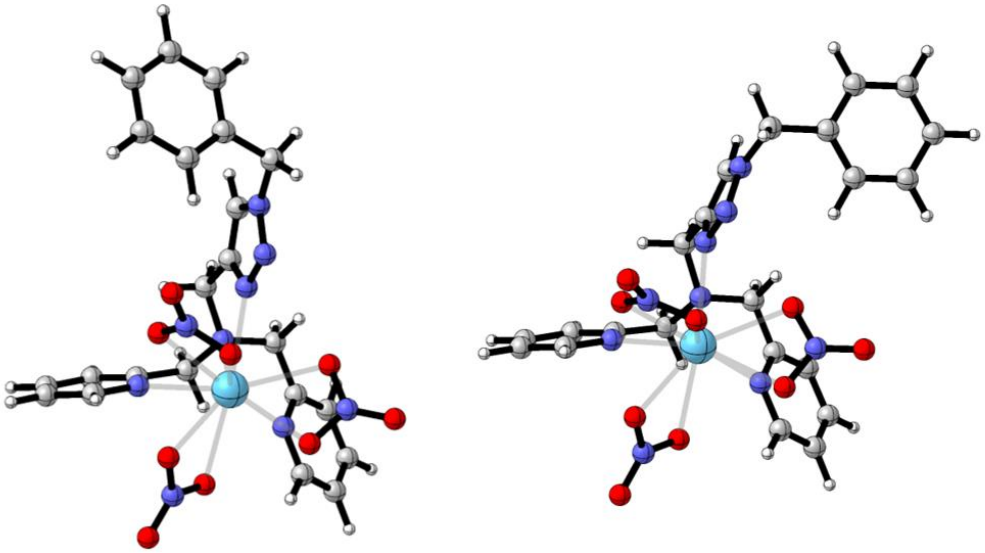

Fig. 6. Lowest-energy conformer (left) and the first higher-energy conformer (right) of **La-1**.

For **La-1**, the optimized geometrical parameters, bond lengths and angles, obtained from DFT calculations are given in Table 1.

Table 1. Bond distances (Å) and angles (°) for **La-1**, as calculated by SHELXL [ref], and their comparison to the simulated data obtained for the lowest-energy conformer (1) and the first higher-energy conformer (2) from DFT calculations (arbitrary atom-numbering scheme used in Figure 1).

	Crystal structure		*Simulated conformer 1*		*Simulated conformer 2*	
Atoms	**Distance (Å)**	**Average (Å)**	**Distance (Å)**	**Average (Å)**	**Distance (Å)**	**Average (Å)**
La1---N1	2.7049(19)	2.7251(93)	2.7055	2.7837 ± 0.069	2.7103	2.7900 ± 0.076
La1---N4	2.7576(17)		2.8963		2.9063	
La1---N5	2.7463(19)		2.7585		2.7374	
La1---N6	2.6919(18)		2.7745		2.8063	
La1---O1	2.5922(16)	2.5816(51)	2.6260	2.6479 ± 0.018	2.5891	2.6497 ± 0.027
La1---O3	2.5753(17)		2.6721		2.6599	
La1---O4	2.6011(18)		2.6443		2.6565	
La1---O6	2.5831(17)		2.6664		2.6674	
La1---O7	2.5709(17)		2.6248		2.6640	
La1---O9	2.5672(18)		2.6539		2.6616	
Atoms	**Angle (°)**	**Average (°)**	**Angle (°)**	**Average (°)**	**Angle (°)**	**Average (°)**
N1---La1---N4	60.36(6)	61.23(9)	60.37	60.15 ± 0.16	61.76	60.67 ± 0.81
N4---La1---N5	61.45(6)		60.08		60.47	
N4---La1---N6	61.89(5)		59.99		59.80	
O1---La1---O3	49.08(5)	49.22(6)	50.17	50.22 ± 0.17	50.68	50.16 ± 0.37
O4---La1---O6	49.02(6)		50.04		49.85	
O7---La1---O9	49.56(6)		50.44		49.96	

Inspection of the conformations revealed a different orientation of the two pyridine rings with respect the central N4 nitrogen atom for both conformers. The dihedral angles around the $PyCH_2$-N4 bond are 175.0° and 68.9° respectively (conf 1), thus placing the two pyridine rings nearly orthogonal to each other. In this arrangement, the triazole ring is almost parallel to one pyridine and perpendicular to the other one. The two conformers principally differ for the relative orientation of the benzyl ring. As highlighted in Figure 7, the lowest-energy conformer has almost the same conformation of the crystallographic structure, with a calculated rmsd of 0.421 Å.

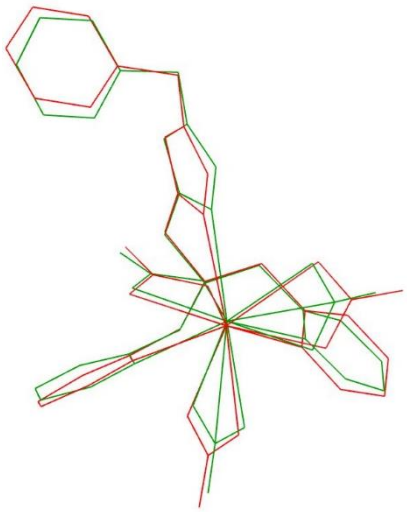

Fig. 7. Overlay of the crystalline geometry of **La-1** (green) onto the lowest-energy conformer (red).

3.5 ^{1}H NMR studies

The formation of the complex in solution was investigated by ^{1}H NMR. In particular, to determine the stoichiometry, titration experiments of the ligand with $La(NO_2)_3$ were performed in deuterated acetonitrile. The progressive addition of $La(NO_2)_3$ (0.5 M in CD_3CN) in aliquots of 0.25 equivalents to a 0.01 M solution of **1** dissolved in CD_3CN led to the gradual disappearance of the resonances of the free ligand and the

appearance of resonances corresponding to the metal complex (see Supplementary Material). In this process, a minor broadening of the signals was detected. After the addition of 1 equivalent, a new single species was observed, and upon the further addition of the lanthanide salt (up to 2 equivalents), no other species were detected. This finding supported the formation of a stable 1:1 ligand/La^{3+} ion complex in CD_3CN solution, as shown in Figure 8, where the spectra of the free ligand and its La(III) complex are reported. The small broadening of the signals during the formation of the complex can be interpreted as a slow exchange process, associated with a strong coordination between the ligand and the metal cation.

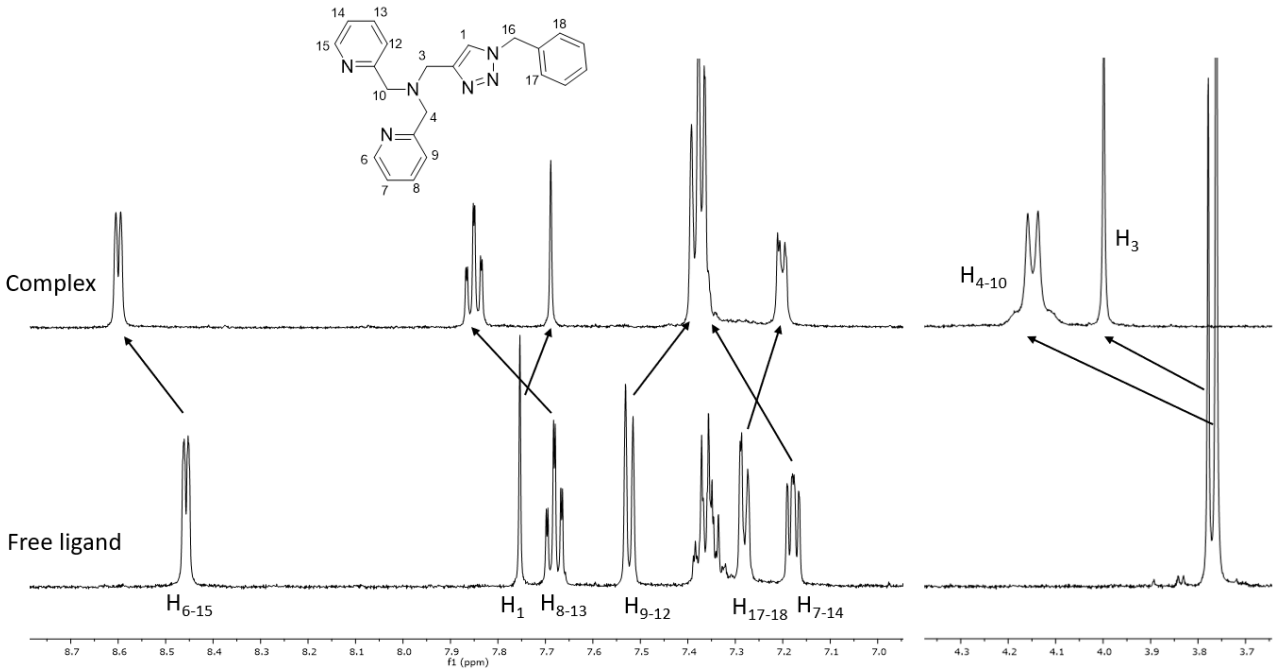

Fig. 8. Expansion of the aromatic (left) and aliphatic (right) regions of the ^1H NMR spectra related to the titration performed dissolving **1** in CD_3CN 0.01 M with $La(NO_2)_3$.

As expected, the signals ascribed to the hydrogen atoms near the coordinating centers of the ligand are shifted downfield (see Table 2). The most evident shifts are for the proton in the aliphatic section. The methylene hydrogens near the triazole ring are shifted by 0.22 ppm, while the ones adjacent to the pyridine rings are found at 0.38 ppm downfield. These last hydrogen atoms are singlets in the spectrum of the free ligand, whereas in the complex they appear as a tight *AB* system (J = 13.9 Hz). This change in the signal shape can be interpreted as a rigidification of the structure around the central metal atom, thus limiting the free mobility of the pyridine rings. The chemical shifts of the pyridine hydrogens also move downfield, except for $H_{9\text{-}12}$. Other signals are shifted upfield, the triazole hydrogen H_1 and the aromatic $H_{17\text{-}18}$ of the benzyl portion: most probably these shifts are the effect of the anisotropy of the aromatic moieties.

Table 2. List of the Δδ (ppm) between **1** and **La-1** (positive values are related to downfield shifts and negative values to upfield shifts). Hydrogen numbering is shown in Figure 8

	$H_{6\text{-}15}$	$H_{7\text{-}14}$	$H_{8\text{-}13}$	$H_{9\text{-}12}$	$H_{4\text{-}10}$	H_3	H_1	H_{16}	$H_{17\text{-}18}$
Δδ (ppm)	0.14	0.19	0.17	-0.15	0.38	0.22	-0.07	-0.01	-0.09

4. Fluorescence analysis

As a part of our studies, the fluorescence properties of **1** and **La-1** were investigated in acetonitrile. To a 10^{-4} M solution of the ligand was added $La(NO_3)_3$ up to 10 equivalents.

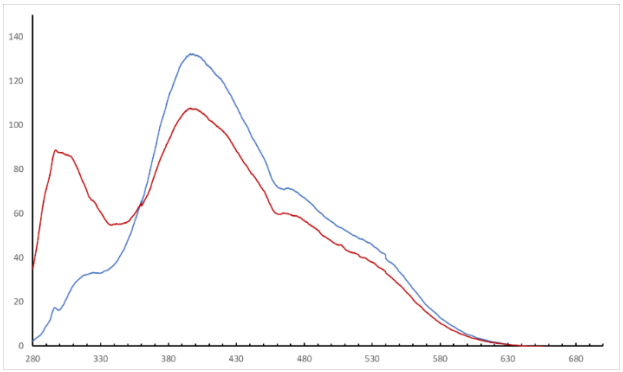

Fig. 8. Fluorescence emission spectra of **1** (5×10^{-5} mol L^{-1}) in CH_3CN (3 mL), shown in blue. Fluorescence changes observed upon addition 10 eq of La^{3+} were reported in red. The spectra were recorded under λ_{ex} = 300 nm, with a 5 nm slit for both excitation and emission.

The ligand was characterized, upon excitation at λ_{ex} = 300 nm, by an emission band around 403 nm in acetonitrile. After addition of an excess of $La(NO_3)_3$, the band at 403 nm decreased, while a new band at 301 nm appeared, with similar intensity. These findings showed that the complex exhibits an enhanced emission intensity about five folds higher with respect to the ligand itself.

To get better insights on the nature of the transitions responsible for the absorption and emission processes, the ligand and the complex were also investigated by means of DFT calculations. To gather information on the orbital involved in the electronic transitions, the highest occupied molecular orbital (HOMO) and lowest unoccupied molecular orbital (LUMO) of **1** and **La-1** were studied. Figure 9 reports the respective energies of HOMO and LUMO orbitals.

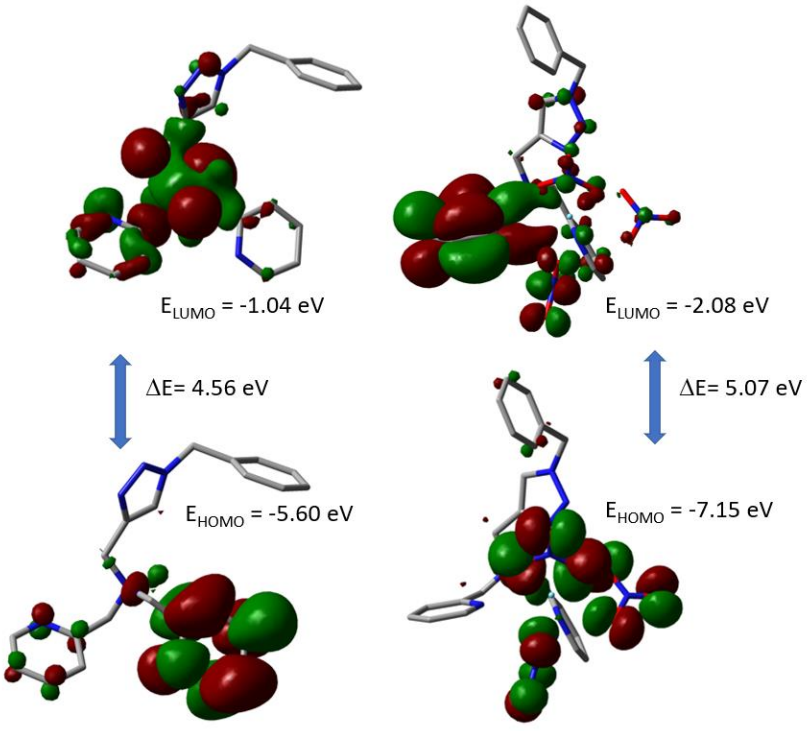

Fig. 9. HOMO and LUMO orbitals for free ligand (left) and the complex (right).

In the ligand, the HOMO orbital is placed on one of the two pyridine rings, whereas the LUMO is mainly centered on the sp^3 central nitrogen atom. The opposite situation is found in the complex, in which the HOMO is located both on the nitrate counter-anions and the sp^3 central nitrogen atom, and the LUMO is positioned on a pyridine ring. The energy gaps are ΔE = 4.56 eV and ΔE = 5.07 eV for the ligand and the

complex, respectively. The shift of the luminescence emission was rationalized in terms of changes in the electron structure as indicated by NMR and DFT calculations, while the significant enhancement of emission was attributed to the increased π conjugation caused by La^{3+} coordination.

5. Conclusions

In this work, ligand 1-(1-benzyl-1*H*-1,2,3-triazol-4-yl)-*N*,*N*-bis(pyridin-2-ylmethyl)methanamine (**1**) afforded *in situ* a new coordination compound with lanthanum nitrate. This novel complex (**La-1**) was deeply investigated by means of SC-XRD, NMR spectroscopy, and theoretical calculations.

La-1 crystallized in the monoclinic system, space group $P2_1/c$, forming with the La(III) ion a deca-coordinated complex. Non-classical C–H···O bonds were the predominant driving forces of the supramolecular assembly. Weak π–π stacking interactions between the pyridines and between the benzyl rings contributed to stabilize the 3D network. The HS of **La-1** evidenced that O···H (~46%), C···H (~27%), and H···H (~18%) contacts constituted an overwhelming majority of the intermolecular interactions. The 2D fingerprint plots confirmed the presence of weak H-bonds and stacking interactions; the propensity to form parallel stacking was further substantiated by the HS mapped over the curvedness. ^{1}HNM titration studies were employed to follow the formation of the complex in solution and identify the correct stoichiometry (1:1 ligand/La^{3+} ion), and DFT analysis proved that the lowest-energy conformer has almost the same conformation of the crystallographic structure.

The fluorescence titration spectra showed that the complex exhibited an enhanced emission intensity about five folds higher with respect to the ligand itself. The mechanism of La(III) coordination was interpreted in terms of electron interaction based on NMR analysis and DFT theoretical calculations, which established a relation between the emission maxima and the HOMO-LUMO energy gap calculated for the complex.

To conclude, our study indicated that **1** is a potential fluorescence sensor, paving the way for the design of new tools for the detection of lanthanide metal ions in environmental chemistry.

Appendix A. Supplementary Material

Supplementary data are available at:

CCDC entry 2058917 number contains the supplementary crystallographic data for this paper. These data can be obtained free of charge via www.ccdc.cam.ac.uk/conts/retrieving.html (or from the Cambridge Crystallographic Data Centre, 12, Union Road, Cambridge CB21EZ, UK; fax: ++44 1223 336 033; or deposit@ccdc.cam.ac.uk).

Author Contributions

Matteo Mori: Investigation, writing - original draft, review & editing. Greta Colombo Dugoni: Investigation. Valentina Dichiarante: Investigation, Review & editing. Alessandro Sacchetti: conceptualization, writing - original draft, review & editing. Fiorella Meneghetti: conceptualization, investigation, writing - original draft, review & editing.

Declaration of Competing Interest

The authors declare that they have no known competing financial interests or personal relationships that could have appeared to influence the work reported in this paper.

Acknowledgments

We acknowledge the University of Milan and the Polytechnic University of Milan for financial support.

References

[1] S. Von Tucher, U. Schmidhalter, Lanthanum uptake from soil and nutrient solution and its effects on plant growth, J. Plant Nutr. Soil Sci. 168 (2005) 574–580. https://doi.org/10.1002/JPLN.200520506.

[2] E. Agathokleous, M. Kitao, E.J. Calabrese, The rare earth element (REE) lanthanum (La) induces hormesis in plants, Environ. Pollut. 238 (2018) 1044–1047. https://doi.org/10.1016/J.ENVPOL.2018.02.068.

[3] G.J. Behets, K.V. Mubiana, L. Lamberts, K. Finsterle, N. Traill, R. Blust, P.C. D'Haese, Use of lanthanum for water treatment A matter of concern?, Chemosphere. 239 (2020) 124780. https://doi.org/10.1016/J.CHEMOSPHERE.2019.124780.

[4] A.J. Hutchison, R.J. Wilson, S. Garafola, J.B. Copley, Lanthanum carbonate: safety data after 10 years, Nephrology. 21 (2016) 987–994. https://doi.org/10.1111/NEP.12864.

[5] A. Granados, I. Rivilla, F.P. Cossío, A. Vallribera, Lanthanum-Catalyzed Enantioselective Trifluoromethylation by Using an Electrophilic Hypervalent Iodine Reagent, Chem. – A Eur. J. 25 (2019) 8214–8218. https://doi.org/10.1002/CHEM.201900598.

[6] K.T. Rim, K.H. Koo, J.S. Park, Toxicological Evaluations of Rare Earths and Their Health Impacts to Workers: A Literature Review, Saf. Health Work. 4 (2013) 12–26. https://doi.org/10.5491/SHAW.2013.4.1.12.

[7] I.G. Nikolov, N. Joki, S. Vicca, N. Patey, D. Auchère, J. Benchitrit, J.P. Flinois, M. Ziol, P. Beaune, T.B. Drüeke, B. Lacour, Tissue Accumulation of Lanthanum as Compared to Aluminum in Rats with Chronic Renal Failure – Possible Harmful Effects after Long-Term Exposure, Nephron Exp. Nephrol. 115 (2010) e112–e121. https://doi.org/10.1159/000313492.

[8] K. De Leeuw, A. Woestenburg, D. Verbeelen, Lanthanum carbonate possibly responsible for acute liver failure in a patient with Child–Pugh stage A liver cirrhosis, NDT Plus. 1 (2008) 412–413. https://doi.org/10.1093/NDTPLUS/SFN137.

[9] E. Slatopolsky, H. Liapis, J. Finch, Progressive accumulation of lanthanum in the liver of normal and uremic rats, Kidney Int. 68 (2005) 2809–2813. https://doi.org/10.1111/J.1523-1755.2005.00753.X.

[10] X. He, Z. Zhang, H. Zhang, Y. Zhao, Z. Chai, Neurotoxicological Evaluation of Long-Term Lanthanum Chloride Exposure in Rats, Toxicol. Sci. 103 (2008) 354–361. https://doi.org/10.1093/TOXSCI/KFN046.

[11] W. Yongxing, W. Xiaorong, H. Zichun, Genotoxicity of lanthanum (III) and gadolinium (III) in human peripheral blood lymphocytes, Bull. Environ. Contam. Toxicol. 64 (2000) 611–616. https://doi.org/10.1007/S001280000047.

[12] W. Khalid, M.A. Abbasi, M. Ali, J. Ahmad, Z. Ali, M. Atif, W. Ensinger, Selective detection of preferential activity of Lanthanum ion at zinc oxide functionalized nanochannel, Nanotechnology. 32 (2021) 245501. https://doi.org/10.1088/1361-6528/ABEC08.

[13] Y. Liu, L. Sun, P. Zhang, J. Wan, R. Wang, J. Xu, Lanthanum inhibits primary root growth by repressing auxin carrier abundances in arabidopsis, Front. Plant Sci. 8 (2017) 1661. https://doi.org/10.3389/FPLS.2017.01661/BIBTEX.

[14] J. Li, R.A. Verweij, C.A.M. van Gestel, Lanthanum toxicity to five different species of soil invertebrates in relation to availability in soil, Chemosphere. 193 (2018) 412–420. https://doi.org/10.1016/J.CHEMOSPHERE.2017.11.040.

[15] H. Herrmann, J. Nolde, S. Berger, S. Heise, Aquatic ecotoxicity of lanthanum – A review and an attempt to derive water and sediment quality criteria, Ecotoxicol. Environ. Saf. 124 (2016) 213–238. https://doi.org/10.1016/J.ECOENV.2015.09.033.

[16] S.I. Presolski, V. Hong, S.H. Cho, M.G. Finn, Tailored ligand acceleration of the cu-catalyzed azide-alkyne cycloaddition reaction: Practical and mechanistic implications, J. Am. Chem. Soc. 132 (2010) 14570–14576. https://doi.org/10.1021/JA105743G.

[17] B. Xu, W. Zhong, Z. Wei, H. Wang, J. Liu, L. Wu, Y. Feng, X. Liu, Iron(III) complexes of multidentate pyridinyl ligands: synthesis, characterization and catalysis of the direct hydroxylation of benzene, Dalt. Trans. 43 (2014) 15337–15345. https://doi.org/10.1039/C4DT02032D.

[18] A. Sacchetti, C. Urra Mancilla, G. Colombo Dugoni, Synthesis of DPA-triazole structures and their application as ligand for metal catalyzed organic reactions, Tetrahedron. 104 (2022) 132581. https://doi.org/10.1016/J.TET.2021.132581.

[19] A.L. Moore, D.K. Buar, L.R. MacGillivray, P.D. Benny, "Click" labeling strategy for M(CO)3 (M = Re, 99mTc) prostate cancer targeted Flutamide agents, Dalt. Trans. 39 (2010) 1926–1928. https://doi.org/10.1039/B921413E.

[20] L. Manzoni, A. Samela, S. Barbini, S. Cairati, M. Penconi, D. Arosio, D. Lecis, P. Seneci, 4-Connected azabicyclo[5.3.0]decane Smac mimetics-Zn2+ chelators as dual action antitumoral agents, Bioorg. Med. Chem. Lett. 27 (2017) 2336–2344. https://doi.org/10.1016/J.BMCL.2017.04.032.

[21] T. Darshani, T.K. Weldeghiorghis, F.R. Fronczek, T. Perera, The first structurally characterized sulfonamide derivatized Zn(II)-dipicolylamine complexes with eight membered chelate rings. Synthetic and structural studies, J. Mol. Struct. 1216 (2020) 128310. https://doi.org/10.1016/J.MOLSTRUC.2020.128310.

[22] G. Wang, C. Platas-Iglesias, G. Angelovski, Europium(III) Macrocyclic Chelates Appended with Tyrosine-based Chromophores and Di-(2-picolyl)amine-based Receptors: Turn-On Luminescent Chemosensors Selective to Zinc(II) Ions, Chempluschem. 85 (2020) 806–814. https://doi.org/10.1002/CPLU.201900731.

[23] A. Rossetti, S. Landoni, F. Meneghetti, C. Castellano, M. Mori, G. Colombo Dugoni, A. Sacchetti, Application of chiral bi- and tetra-dentate bispidine-derived ligands in the copper(ii)-catalyzed asymmetric Henry reaction, New J. Chem. 42 (2018) 12072–12081. https://doi.org/10.1039/C8NJ01930D.

[24] M. Lippi, J. Caputo, A. Famulari, A. Sacchetti, C. Castellano, F. Meneghetti, J. Martí-Rujas, M. Cametti, Combined structural and theoretical investigation on differently substituted bispidine ligands: predicting the properties of their corresponding coordination polymers, Dalt. Trans. 49 (2020) 5965–5973. https://doi.org/10.1039/D0DT00799D.

[25] O. Alptü Rk, O. Rusin, S.O. Fakayode, W. Wang, J.O. Escobedo, I.M. Warner, W.E. Crowe, V. Krá, J.M. Pruet, R.M. Strongin, Lanthanide complexes as fluorescent indicators for neutral sugars and cancer biomarkers, Proc. Natl. Acad. Sci. 103 (2006) 9756–9760. https://doi.org/10.1073pnas.0603758103.

[26] Q. Zhao, X.M. Liu, H.R. Li, Y.H. Zhang, X.H. Bu, High-performance fluorescence sensing of lanthanum ions (La3+) by a polydentate pyridyl-based quinoxaline derivative, Dalt. Trans. 45 (2016) 10836–10841. https://doi.org/10.1039/C6DT01161F.

[27] S. Huang, R.J. Clark, L. Zhu, Highly sensitive fluorescent probes for zinc ion based on triazolyl-containing tetradentate coordination motifs, Org. Lett. 9 (2007) 4999–5002. https://doi.org/10.1021/OL702208Y.

[28] SAINT software reference manual, Bruker AXS, Madison, WI. 5465 (1998).

[29] S. Parkin, B. Moezzi, H. Hope, IUCr, XABS2: an empirical absorption correction program, J. Appl. Crystallogr. 28 (1995) 53–56. https://doi.org/10.1107/S0021889894009428.

[30] M.C. Burla, R. Caliandro, B. Carrozzini, G.L. Cascarano, C. Cuocci, C. Giacovazzo, M. Mallamo, A.

Mazzone, G. Polidori, Crystal structure determination and refinement via SIR2014, J. Appl. Crystallogr. 48 (2015) 306–309. https://doi.org/10.1107/S1600576715001132.

[31] G.M. Sheldrick, Crystal structure refinement with SHELXL, Acta Crystallogr. Sect. C Struct. Chem. 71 (2015) 3–8. https://doi.org/10.1107/S2053229614024218.

[32] L.J. Farrugia, WinGX and ORTEP for Windows: an update, J. Appl. Crystallogr. 45 (2012) 849–854. https://doi.org/10.1107/S0021889812029111.

[33] M. Nardelli, PARST95 – an update to PARST: a system of Fortran routines for calculating molecular structure parameters from the results of crystal structure analyses, J. Appl. Crystallogr. 28 (1995) 659–659. https://doi.org/10.1107/S0021889895007138.

[34] C.F. MacRae, I. Sovago, S.J. Cottrell, P.T.A. Galek, P. McCabe, E. Pidcock, M. Platings, G.P. Shields, J.S. Stevens, M. Towler, P.A. Wood, Mercury 4.0: from visualization to analysis, design and prediction, J. Appl. Crystallogr. 53 (2020) 226–235. https://doi.org/10.1107/S1600576719014092.

[35] P.R. Spackman, M.J. Turner, J.J. McKinnon, S.K. Wolff, D.J. Grimwood, D. Jayatilaka, M.A. Spackman, CrystalExplorer: a program for Hirshfeld surface analysis, visualization and quantitative analysis of molecular crystals, J. Appl. Crystallogr. 54 (2021) 1006–1011. https://doi.org/10.1107/S1600576721002910.

[36] † Silvio Aime, † Alessandro Barge, ‡ Franco Benetollo, *,§ Gabriella Bombieri, † and Mauro Botta, F. Uggeri‖, A Novel Compound in the Lanthanide(III) DOTA Series. X-ray Crystal and Molecular Structure of the Complex Na[La(DOTA)La(HDOTA)]·10H2O, Inorg. Chem. 36 (1997) 4287–4289. https://doi.org/10.1021/IC9704501.